Author/s:
Wu, Y;Stewart, AG;Lee, PVS

Title:
High-throughput microfluidic compressibility cytometry using multi-tilted-angle surface acoustic wave

Date:
2021-07-21

Citation:
Wu, Y., Stewart, A. G. & Lee, P. V. S. (2021). High-throughput microfluidic compressibility cytometry using multi-tilted-angle surface acoustic wave. Lab on A Chip, 21 (14), pp.2812-2824. https://doi.org/10.1039/d1lc00186h.

Persistent Link:
https://hdl.handle.net/11343/355933

Title

High-throughput microfluidic compressibility cytometry using multi-tilted-angle surface acoustic wave

Yanqi Wu[1], Alastair G. Stewart[2,3] and Peter V.S. Lee[1]

[1]Department of Biomedical Engineering, University of Melbourne, Melbourne, VIC 3010, Australia

[2]Department of Biochemistry and Pharmacology, University of Melbourne, Melbourne, VIC 3010, Australia

[3]ARC Centre for Personalised Therapeutics Technologies, Melbourne, VIC 3010, Australia

Corresponding author:

Peter V.S. Lee,

Department of Biomedical Engineering, University of Melbourne, Melbourne, Australia

Email: pvlee@unimelb.edu.au

1

Abstract

Cellular mechanical properties (*e.g.* compressibility) are important biophysical markers in relation to cellular processes and functionality. Among the methods for cell mechanical measurement, acoustofluidic methods appear to be advantageous due to tunability, biocompatibility and acousto-mechanical nature. However, the previous acoustofluidic methods were limited in throughput and number of measurements. In this study, we developed a high-throughput microfluidic compressibility cytometry approach using multi-tilted-angle surface acoustic wave, which can provide thousands of single-cell compressibility measurements within minutes. The compressibility cytometer was constructed to drag microparticles or cells towards the microfluidic channel sidewall at different segments based on their biophysical properties (such as size and compressibility), as a result of the varied balance between acoustics and flow. Mathematical analysis and computational simulation revealed that the compressibility of a cell could be estimated from the position of collision with the sidewall. Microbeads of different materials and sizes were experimentally tested to validate the simulation and to demonstrate the capability to characterise size and compressibility. MDA MB231 cells, of the triple negative breast cancer subtype, were treated with the microtubule disrupting agent colchicine which increased compressibility and treated with the actin disrupting agent cytochalasin which increased cell size but did not change compressibility. Moreover, the highly metastatic variant MDA MB231 LNm5 cell line showed increased compressibility than the parent MDA MB231 cells, indicating the potential utility of high-throughput mechanophenotyping for tumour cell characterisation.

1 Introduction

Cells are dynamic, living structures that remodel in response to stimuli from environment or in relation to intrinsic processes such as cell growth, proliferation, differentiation, migration and death.[1–4] The mechanical properties of cells have been repeatedly probed as biophysical indicators based on the correlation between these biological processes and the associated cell mechanics.[5,6] In addition, many diseases associate with mechanical irregularities in cell mechanics, such as sickle cell anemia,[7] malaria[8,9] and cancer.[10,11] The changes in cell mechanical properties represent underlying abnormal functionality and can be used for the applications in disease detection, diagnosis and treatment.[12] For example, the deformability of disseminated tumour cells in pleural effusions was used to diagnose pathological states such as acute inflammation and a deformability-based scoring system was established to evaluate the malignancy.[13]

Cell mechanical properties have been conventionally measured by a variety of techniques, such as cell-poking microneedles,[14,15] atomic force microscopy (AFM),[16] micropipette aspiration,[17] optical tweezer,[18] and magnetic tweezer.[19] These conventional techniques provide an effective mechanical measurement of cells and usually give a measure of cellular Young's modulus or shear modulus.[20] However, they often require bulky sophisticated apparatus to probe one cell at a time, and are therefore limited by high instrument cost and low throughput.

The emerging microfluidic methods provide a solution that promises low-cost and high-throughput manner.[21] To date, a variety of microfluidic applications have been developed for cell mechanical measurement, based on the deformation induced by hydrodynamic stress,[22–24] physical contact with microchannel,[25–27] and external force fields such as optics.[10,28,29] Among the family of microfluidic methods, acoustofluidic method which is the fusion of acoustics and microfluidics appears to be advantageous for cell mechanics applications due to its tunability, biocompatibility and acousto-mechanical nature.[30,31] In particular, acoustofluidic method creates a contact-free force field with a spatial resolution at the same or smaller scale as cells, therefore being capable of probing individual cells.[31–33] Due to the mechanical nature of acoustic waves, the acoustic radiation force exerted on a cell is dependent on its mechanical property, *i.e.* compressibility or bulk modulus, which thereby can be measured through the acoustic radiation force. This method provides an additional mechanical parameter to the more commonly measures of Young's modulus and shear modulus of the cell.[34]

Several studies have implemented acoustofluidic methods for cell mechanical measurement. These studies adopted a trajectory-tracking method, experimentally capturing the trajectory of individual cells driven by the acoustic radiation force and fitting each trajectory with the theoretical prediction for an estimate of acoustic radiation force and thereby cell compressibility. For example, Hartono *et al* measured the compressibility of various cancer cell lines by analysing the trajectory of initially scattering cells being dragged by the acoustic radiation force.[35] Yang *et al* incorporated optical lasers into the acoustofluidic setup, positioning cells at one position and then applying the acoustic radiation force.[28] Wu *et al* further extended the idea using the phase modulation of surface acoustic wave to pre-focus cells in one line before tracking the trajectory towards a new line driven by the acoustic radiation force.[36] These trajectory-tracking methods captured the entire motion of a cell requiring a few seconds and repeated in a batch-wise manner for the following cells. In one batch, the cells were usually tested under no-flow condition or a very slow flow for the purpose of ensuring a complete motion capture. Wang *et al* adjusted the method to a continuous-flow version by measuring a cut-off position in the middle of the cell motion, but the reported measurements were still tens of cells for each population.[37] Hence, the methods have been limited in terms of throughput.

Acoustofluidic method has also been widely exploited in the applications of cell separation, which operate in a continuous-flow and high-throughput manner.[38] The separation was achieved by creating a threshold for different speed towards the acoustic-induced focusing line,[39–41] different motion direction travelling across a tilted acoustic field,[42–44] or different equilibrium position in a medium with certain property value or gradient.[45,46] These differences stem from the significant differences in biophysical properties and therefore in the magnitude of acoustic radiation forces between two populations. However, the separation is binary with a single threshold and shows difficulties when two populations have overlapping properties.[44,46] In addition, it does not provide a measured characteristic of population and its usage is limited to specific applications of two populations that differ in cell size.[38] A recent study attempted to adjust the binary threshold by applying a random sequence of voltages, but could not provide single-cell measurements due to the difficulties in registering the voltages with single-cell detection.[47]

In this study, we developed a high-throughput microfluidic compressibility cytometry method using multi-tilted-angle surface acoustic wave (SAW), which operates under a continuous flow, separates microparticles or cells into different bins based on their biophysical properties and

provides thousands of cell compressibility measurements in a few minutes. The working principle was first demonstrated by mathematical analysis and computational simulation, followed by fabrication of the compressibility cytometric device. Three sets of experiments were done using the compressibility cytometry. Firstly, in order to validate the working principle and to demonstrate the characterisation capability, polymer microbeads of different materials and sizes were tested. Secondly, the compressibility cytometry was used to characterise MDA MB231 cell line in response to drug-induced cellular structure disruption, where the cells treated with colchicine (known to disrupt cellular microtubules) and with cytochalasin B (known to disrupt actin filaments) were characterised. Finally, the compressibility cytometry was used to characterise cell lines with different metastatic phenotypes, where MDA MB231 cells and the highly metastatic variant MDA MB231 LNm5 cells were examined and compared.

2 Working Principle

The multi-tilted-angle surface acoustic wave (SAW) compressibility cytometer device consists of a $LiNbO_3$ piezoelectric substrate and a PDMS microchannel containing a series of segments with different angles with respect to a pair of interdigital transducers (IDTs) deposited on the substrate (Fig. 1a). The device is constructed to separate microparticles or cells into different bins based on their biophysical properties such as size and compressibility, by dragging them towards the sidewalls at different segments (Fig. 1b). This is achieved by the design of channel tilted angles that vary the balance between the effects of acoustics and flow.

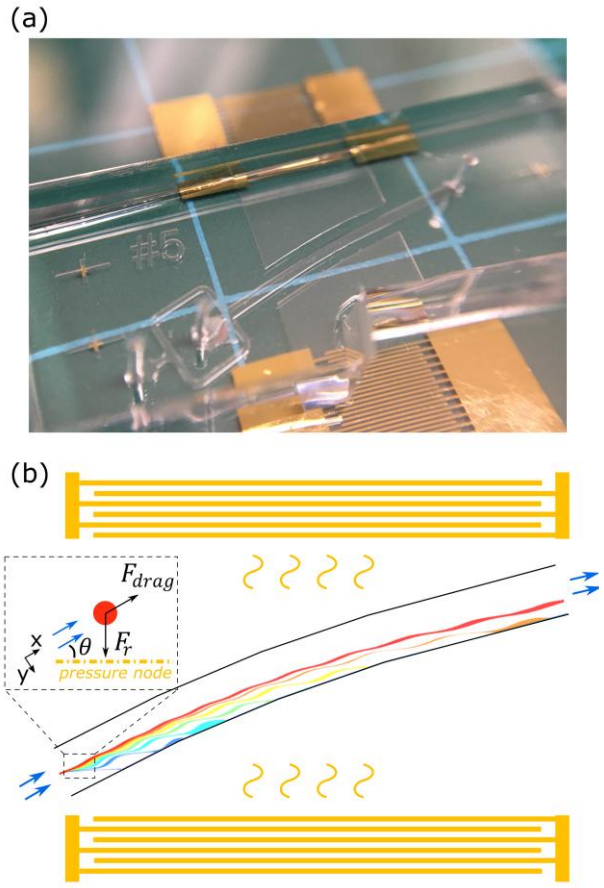

Fig. 1 (a) Photo of compressibility cytometer, consisting of a pair of interdigital transducers (IDTs) on a LiNbO3 piezoelectric substrate and a PDMS microchannel containing a series of segments tilted by different angles. The grid square in the background is 10 mm × 10 mm. (b) Schematic of compressibility cytometer separating microparticles or cells into different bins by dragging them towards the sidewalls at different segments of the microfluidic channel.

2.1 Theory

Once a radio frequency (RF) signal at the resonant frequency is imposed at each IDT, it generates two counter-propagating SAWs traveling from the IDTs in the form of a Rayleigh wave and entering the fluidic domain in the microchannel. A pressure interference is formed in the fluidic domain and the time-averaged pressure creates the acoustic radiation force F_r pushing any particles present towards a pressure node or antinode depending on their acoustic contrast. Most solid polymer microbeads and cells, including the ones used in this study, have a positive acoustic contrast.[31] Hence, the acoustic radiation force F_r would push particles towards pressure nodes and could be defined as below.[48]

$$F_r = -\frac{E_{ac}\pi V_p \beta_m}{2\lambda} \cdot \left(\frac{5\rho_P - 2\rho_m}{2\rho_P + \rho_m} - \frac{\beta_P}{\beta_m} \right) \cdot \sin(2kd) \tag{1a}$$

$$E_{ac} = \frac{\alpha V_I^2 \rho_s c_s}{A_w} \tag{1b}$$

where E_{ac} denotes the acoustic energy intensity; ρ_P , β_P and V_p denotes the density, compressibility and volume of the particle respectively; ρ_m and β_m denotes the density and compressibility of the medium repectively; ρ_s and c_s denotes the density and acoustic velocity within substrate respectively; d denotes the distance away from pressure node and $d = 0$ coincides with pressure node; λ and k denotes the wavelength and the wavenumber of acoustic wave respectively; V_I dentoes the input voltage to the IDT; A_w denotes the working area of IDT; α denotes the energy coefficient.

Another governing force on the particle is the well-known Stoke's drag force from the fluid.

$$F_{drag} = -6\mu\pi R v_{rel} \tag{2}$$

where μ denotes the dynamic viscosity; R denotes the radius of the particle; v_{rel} denotes the particle velocity relative to that of the flow.

The motion of a particle can therefore be described by the balance between the acoustic radiation force F_r and Stoke's drag force F_{drag} along the x- and y-directions.

$$\begin{cases} \dfrac{E_{ac}\pi V_p \beta_m}{2\lambda} \cdot \left(\dfrac{5\rho_P - 2\rho_m}{2\rho_P + \rho_m} - \dfrac{\beta_P}{\beta_m}\right) \cdot sin(2kd) \cdot sin\,\theta + 6\mu\pi R\left[\dfrac{dx}{dt} - v_0(y)\right] = 0 \\ \dfrac{E_{ac}\pi V_p \beta_m}{2\lambda} \cdot \left(\dfrac{5\rho_P - 2\rho_m}{2\rho_P + \rho_m} - \dfrac{\beta_P}{\beta_m}\right) \cdot sin(2kd) \cdot cos\,\theta + 6\mu\pi R\dfrac{dy}{dt} = 0 \end{cases} \tag{3}$$

where θ denotes the angle between acoustic-induced pressure node and flow direction; $v_0(y)$ denotes the flow velocity profile, which is a function of y since the channel is along the x-direction and under laminar condition.

In order to have a clearer representation of particle trajectory, eqn (3) can be combined and transformed as below.

$$\frac{dy}{dx} = \frac{-C\dfrac{V_I^2}{Q} \cdot \psi \cdot \sin[2k(x\sin\theta + y\cos\theta)] \cdot \cos\theta}{-C\dfrac{V_I^2}{Q} \cdot \psi \cdot \sin[2k(x\sin\theta + y\cos\theta)] \cdot \sin\theta + u(y)} \tag{4a}$$

$$C \overset{\text{def}}{=} \frac{\pi\alpha\rho_s c_s \beta_m}{9\mu\lambda A_w} \tag{4b}$$

$$\psi \overset{\text{def}}{=} R^2 \cdot \left(\frac{5\rho_P - 2\rho_m}{2\rho_P + \rho_m} - \frac{\beta_P}{\beta_m}\right) \tag{4c}$$

where Q denotes the flow rate; $u(y)$ denotes the flow velocity profile per unit flow rate, that is, $v_0(y) = Q \cdot u(y)$, which is also constant once the microchannel dimension is determined.

We define a constant C specific to the device and the testing medium which is water or aqueous solution throughout this study, and a combined property ψ for the particle in eqn (4). This indicates that the particle trajectory depends on experimental conditions such as input voltage V_I and flow rate Q and particle properties including radius R, density ρ_P and compressibility β_P.

2.2 Multi-tilted angle simulation

A scenario of one tilted angle was first analysed to demonstrate the angle-dependent thresholding effect on particle properties and to assist the tilted angle design. In the simulation, particles flowing from the centre of a single straight channel titled at an angle were subjected to a constant flow and acoustic radiation force. The particle trajectory was simulated by solving eqn (4) using MATLAB (R2017a, MathWorks) and the lateral displacement was calculated. The simulation covered a range of tilted angle θ and a range of particle compressibility β_P, while the other parameters were fixed including the medium as water, the particle as MCF-7 cell reported in the previous study[36] and the microchannel dimension as 450 μm in width and 1000 μm in length.

Then multi-tilted angle is conceptualised with a series of straight segments in sequence with varied tilted angles, such that particles will be separated into groups hitting the sidewall of the segment where their properties match the threshold (Fig. 1b). The particle trajectory in a multi-tilted-angle device can be simulated by repeatedly solving eqn (4) using MATLAB (R2017a, MathWorks). Based on eqn (4), the simulation results can be represented as a map of hitting position $H = H\left(C\frac{V_I^2}{Q}, \psi\right)$, which is a function of parameter $C\frac{V_I^2}{Q}$ related to experimental conditions and particle property ψ related to size, density and compressibility. Hitting position $H = 1,2,3,\ldots,n$ refers to channel segment number 1 to n where particles hit the sidewall. Hitting position $H = n + 1$ means particles do not hit the sidewall. There are few situations at the transition from one segment to another that hitting position H is a fractional number, because the pre-focused band of particles split into hitting two neighbouring segments due to the slight difference in initial position. In this case, hitting position H is defined as the mean hitting position of the band. More information about multi-tilted-angle simulation can be found in the ESI.

2.3 Compressibility measurement

When a population of particles are tested, they are injected into the multi-tilted-angle SAW device, hydrodynamically focused and then subjected to both acoustics and flow. The motion of each particle is video recorded, in which the hitting position H and radius R is captured by image analysis. Knowing the input voltage V_I, flow rate Q and device constant C (obtained from calibration process), the captured hitting position H can be converted to an estimate of property ψ in eqn (4c) using the simulated hitting position map $H = H\left(C\frac{V_I^2}{Q}, \psi\right)$. The property ψ is defined based on radius R, density ρ_P and compressibility β_P . In this study, the density of microbeads is obtained from literature and that of cells is assumed to be a constant value of 1050 kgm^{-3} supported by previous studies.[36,49–51] The radius R is experimentally captured from video recordings. Hence, by decoupling radius R and density ρ_P, the estimated property ψ can be further converted to an estimate of compressibility β_P for each particle. In the hitting position map, a hitting position H may lead to a small range of ψ values and therefore a small interval for compressibility β_P, so the median of compressibility interval is used as the estimate.

3 Materials and Methods

3.1 Fabrication and calibration

The fabrication process has been previously described.[36] The device comprises of a PDMS microchannel and a $LiNbO_3$ piezoelectric substrate. The PDMS microchannel has a main inlet for sample, a sheath inlet for hydrodynamic focus before acoustic area and an outlet. An array of pillars with the minimal spacing of 20 μm is designed right after the main inlet, for the purpose of filtering out larger dusts or aggregates and only allowing single microbead or cell entering the channel. The channel consists of segments with a length of 1000 μm, a width of 450 μm for each and a uniform height of 100 μm. This single-layer PDMS microchannel was fabricated using the standard soft lithography and PDMS casting techniques. On the other hand, a 128° Y-cut X-propagation $LiNbO_3$ wafer was used to build the piezoelectric substrate. A pair of IDTs were deposited on the $LiNbO_3$ substrate using the lift-off process with uniform electrode width and spacing of both 75 μm, leading to a resonant frequency of ~12.8 MHz. Then the PDMS channel and $LiNbO_3$ substrate were aligned and bonded by air plasma. The calibration process of a fabricated device can be found in the ESI.

3.2 System setup

The device was mounted on an inverted microscope (IX51, Olympus) with a digital monochrome camera (BM-141GE, JAI cameras). The main inlet and sheath inlet were connected to two glass syringes (1001TLL, Hamilton) driven by two syringe pumps (Legato 180 and Legato 270, KD Scientific) via PTFE tubing, respectively. A signal generator (DG-4102, RIGOL) provided a RF signal which was sequentially amplified by a RF power amplifier to the two IDTs. An oscilloscope (DS-1102E, RIGOL) was used to monitor the real-time voltage provided to the IDTs to ensure a stable input voltage to the device as desired. A custom LabVIEW program was used to control the signal generator, monitor the input voltage to the device and acquire the real-time images from the camera.

3.3 Sample preparation

MDA MB231 cells [American Type Culture Collection (ATCC)] were cultured in a complete DMEM medium [containing 10% (v/v) HIFCS, 2mM L-Glutamine, 1% (v/v) non-essential amino acids, 1% (v/v) sodium pyruvate, 0.2% (v/v) sodium bicarbonate, 15mM HEPES, 100IU/ml penicillin and 50 µg/ml streptomycin] and kept in an humidified incubator at 37°C and containing 5% CO_2. The cells were passaged twice weekly by PBS wash, trypsinization, centrifugation and resuspension in complete DMEM.

MDA MB231 LNm5 cells were derived through a process as previously described.[52] A cell population kindly provided by ZM Shao and ZL Ou (Breast Cancer Institute, Fudan University, Shanghai, China)[53] were inoculated into the mammary fat pad of a female BALB/c-SCID mouse, followed by the isolation of axillary lymph node metastases as described in a transcriptomic comparison of these two cell lines.[54] These cell lines were cultured as described in the study of Johnstone *et al*.[54]

In the drug treatment experiment, colchicine that is known to disrupt microtubules[36] was added to MDA MB231 cells at 1, 10 or 100 µM. Cytochalasin B that is known to disrupt actin filaments[55] was added to MDA MB231 cells at 1, 3 or 10 µM. Then the cells were kept in the incubator at 37°C in a humidified atmosphere of 5% CO_2 for 4 hours.

Before the experiment, the device was primed with PBS containing 0.25% BSA and 0.3% Pluronic F127 for the purpose of clearing air in the microfluidic channel. In the microbead experiment, 10-µm PS microbeads (Magsphere), 10-µm PMMA microbeads (PolyAn) and 15-µm PS microbeads (Advance Scientific) were prepared in Milli-Q water containing 0.3% Pluronic F127 at the concentration of ~2×10^6/ml and injected into the main inlet, while Milli-

Q water was injected into the sheath inlet. In the cell experiment, cells were washed with PBS, trypsinized, sedimented by centrifugation, resuspended in PBS at the concentration of 1 – 1.5 × 10^6/ml and injected into the main inlet, while PBS was injected into the sheath inlet. The flow rate ratio of main inlet to sheath inlet was kept at 1:10.

4 Results

4.1 Device design and simulation

In the first simulation for the angle-dependent thresholding effect, particles with varied compressibility from the centre of a single straight channel titled at a varied angle were subjected to a constant flow and acoustic radiation force (Fig. 2a). The simulation results show that less compressible particles reach the maximum lateral displacement (225 μm) and hit the sidewall, while more compressible particles have a small lateral displacement and stay in the centre, indicating a thresholding effect on the particle compressibility. The threshold on compressibility can be tuned by changing the tilted angle, where a decrease in tilted angle will increase the portion of particles hitting the sidewall and *vice versa*.

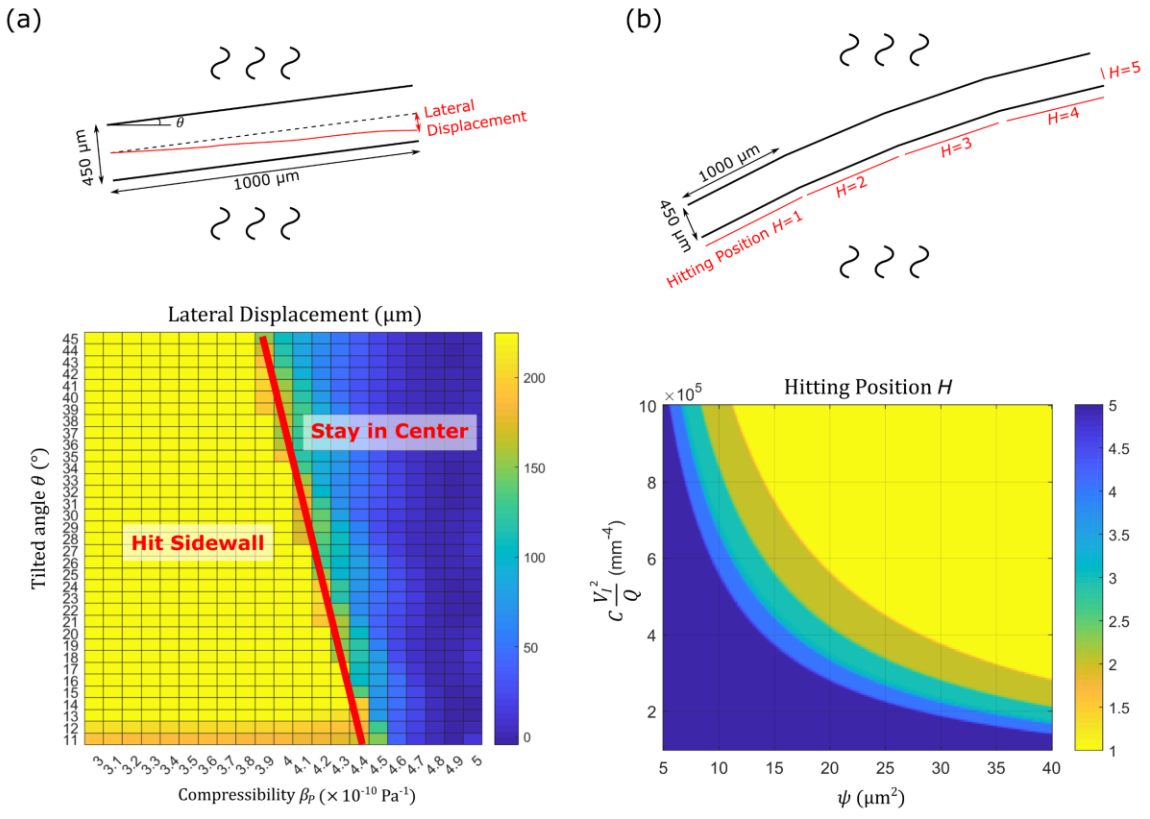

Fig. 2 (a) Simulation of a one-tilted-angle scenario. The lateral displacement was simulated with regard to a range of tilted angle θ and a range of particle compressibility β_P, while the other parameters were fixed. (b) Simulation of multi-tilted-angle compressibility cytometry. The simulated hitting position H is a function of parameter $C\frac{V_I^2}{Q}$ related to a constant C, input voltage V_I and flow rate Q, and particle property ψ related to size, density and compressibility. Results were represented as a hitting position map.

In the second simulation for the multi-tiled-angle SAW device, the microchannel was designed with four straight segments in sequence with decreasing tilted angles, such that a series of thresholds were created to allow particles hitting the sidewall of the segment where their properties match the local threshold. The tilted angles were chosen as 20°, 18°, 16° and 14° throughout this study, based on the simulation results in Fig. 2a compared to the reported cell compressibility.[36] The hitting position H, which had values of $H = 1{\sim}5$, was simulated and represented as a hitting position map (Fig. 2b). The hitting position map suggests that at a certain parameter $C\frac{V_I^2}{Q}$, that is, under a certain input voltage V_I and flow rate Q and with a device constant C, the particles with different property ψ will hit the sidewall at different positions. In practice, the parameter $C\frac{V_I^2}{Q}$ can be tuned by changing the input voltage V_I and/or flow rate Q, leading to a shift in the threshold on the property ψ and therefore size, density or compressibility.

4.2 Measurement of microbeads

Microbeads of different materials and diameters were first tested using the compressibility cytometry, including 10-μm PS, 10-μm PMMA and 15-μm PS microbeads. Each group of microbeads were tested under multiple combinations of input voltage and flow rate, and therefore different values of V_I^2/Q, in order to shift the cut-off threshold and to validate the theory in various conditions. The combinations of input voltage and flow rate, V_I^2/Q, were adjusted for each group while ensuring an effective hitting position between $H = 1$ and $H = 5$.

We observed that the microbeads were dragged towards the sidewall as a result of both acoustics and flow, hitting the sidewall at certain positions (Fig. 3a). ~100 microbeads were tested for each value of V_I^2/Q from each group, and the results were presented as the mean and standard deviation of hitting position for those microbeads (Fig. 3b). For all three groups of microbeads, the mean hitting position decreased when the V_I^2/Q increased, which agrees with the expectation that particles will be dragged towards the sidewall earlier when the acoustics

is stronger and/or the flow is slower. The hitting position of microbeads of different materials or sizes could be seen clearly in the following examples. PS and PMMA microbeads of 10-μm diameter were both tested under V_I^2/Q = 113.6 and 142.5 V^2(μL/min)$^{-1}$ and showed differences in mean hitting position of 3.96 *vs* 1.90 and 2.83 *vs* 1.79, respectively. In addition, for a similar hitting position such as $H = \sim 2$, the three groups of microbeads required different combinations of voltage and flow rate, V_I^2/Q, where 10-μm PS microbeads needed twice the V_I^2/Q and equivalently twice the input power as 15-μm PS microbeads.

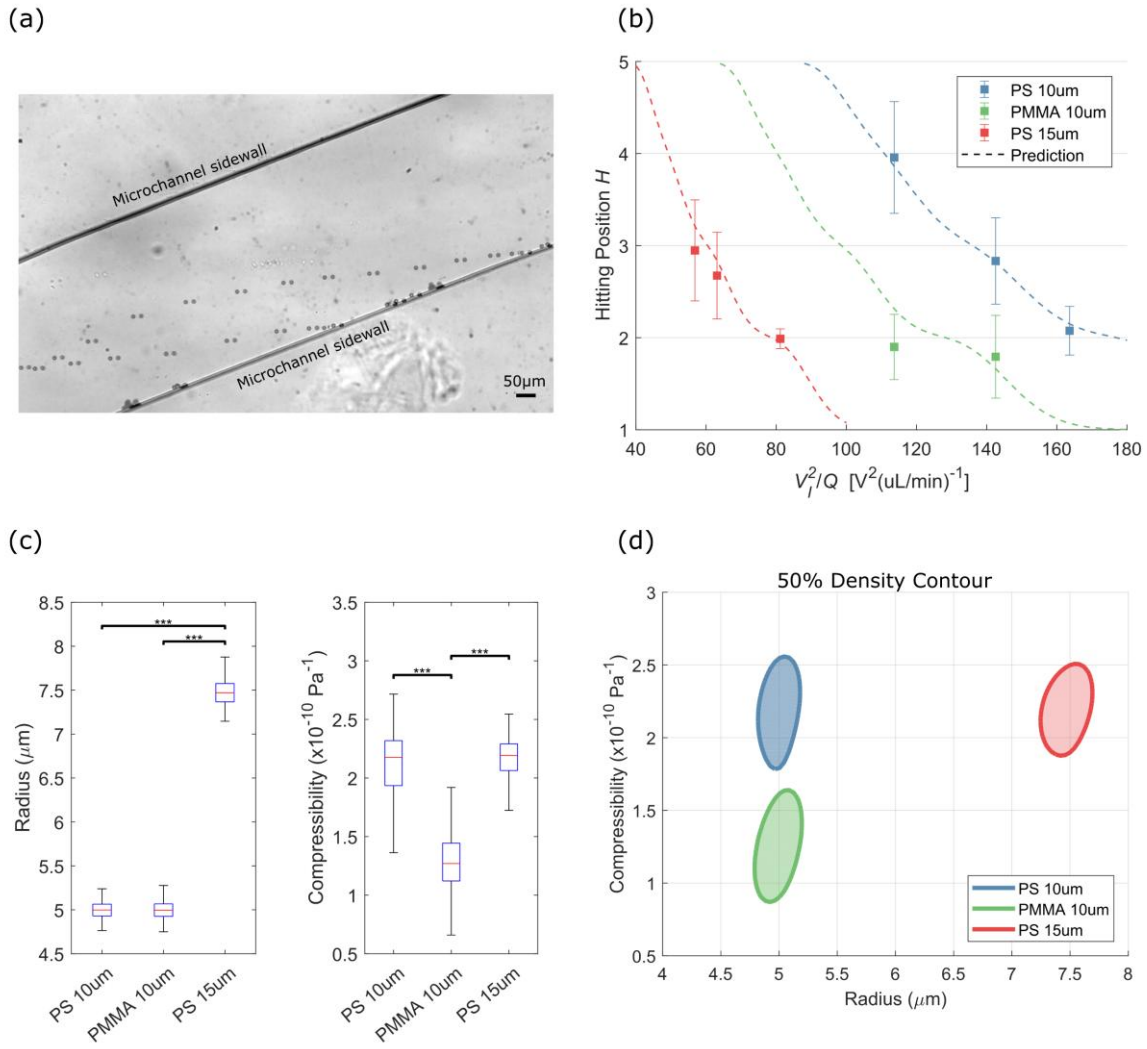

Fig. 3 Measurement of microbeads. (a) Time-lapse overlaid image of two microbeads hitting the sidewall at certain positions as a result of both acoustics and flow. (b) Experimental and predicted hitting positions, (c) measured radius and compressibility, and (d) 50% density contour of compressibility *vs* radius for 10-μm PS (n = 476), 10-μm PMMA (n = 346) and 15-μm PS (n = 314) microbeads. *** denotes $p < 0.001$ (unpaired t-test). Data are represented as mean and standard deviation in (b) and a standard box plot

in (c). The single microbead appeared as double images at every timepoint in (a) due to the uniaxial birefringence of LiNbO3.

Since the properties of PS and PMMA can be found in literature, the hitting positions were predicted using the hitting position map. The property values used for prediction are provided in the ESI. The predicted hitting positions were plotted as dashed lines in Fig. 3b, and the agreement with the experimental results suggests that the proposed theory is reliable.

The radius and compressibility of microbeads were measured by the compressibility cytometry (Fig. 3c) and summarised in Table 1. The measured radius agrees with the specifications from manufacturer, and the measured compressibility agrees with $2.1 – 2.4 \times 10^{-10}$ Pa^{-1} for PS[35,56] and $1.1 – 1.7 \times 10^{-10}$ Pa^{-1} for PMMA.[57,58] These results suggest that the compressibility of PS and PMMA has been correctly characterised by the compressibility cytometry. The 50% density contour of compressibility *vs* radius, which is the probability contour within which 50% of the population resides, was plotted for each group (Fig. 3d). This bivariate contour clearly distinguished 10-μm PS, 10-μm PMMA and 15-μm PS microbeads in terms of the location and spread in the graph, providing further insights on the characteristic of a population. The full data of univariate and bivariate distributions of cell compressibility and size can be found in the ESI.

Experiment	*Sample*	*Radius (μm)*	*Compressibility (× 10^{-10} Pa^{-1})*
Microbeads	10-μm PS	4.99 ± 0.10 (n = 476)	2.10 ± 0.31 (n = 476)
	10-μm PMMA	5.00 ± 0.11 (n = 346)	1.33 ± 0.42 (n = 346)†
	15-μm PS	7.48 ± 0.15 (n = 314)†	2.14 ± 0.22 (n = 314)
Microtubule disruption	Control	7.46 ± 0.85 (n = 1444)	3.56 ± 0.32 (n = 1444)
	Colchicine 1μM	7.41 ± 0.86 (n = 916)	3.61 ± 0.33 (n = 916)*
	Colchicine 10μM	7.47± 0.86 (n = 1013)	3.61 ± 0.33 (n = 1013)*
	Colchicine 100μM	7.61 ± 0.88 (n = 968)*	3.64 ± 0.32 (n = 968)*
Actin disruption	Control	7.19 ± 0.78 (n = 1099)	3.63 ± 0.31 (n = 1099)
	Cytochalasin B 1μM	7.41 ± 0.75 (n = 1016)*	3.61 ± 0.35 (n = 1016)
	Cytochalasin B 3μM	7.53 ± 0.77 (n = 989)*	3.63 ± 0.34 (n = 989)
	Cytochalasin B 10μM	7.45 ± 0.78 (n = 1056)*	3.62 ± 0.36 (n = 1056)
Metastatic potential	MDA MB231	7.38 ± 0.80 (n = 1197)	3.62 ± 0.36 (n = 1197)
	MDA MB231 LNm5	7.57 ± 0.94 (n = 1146)*	3.82 ± 0.30 (n = 1146)*

† denotes that the group has a statistically significant difference with all the other groups in the same experiment ($p < 0.001$, unpaired t-test).

* denotes that the group has a statistically significant difference with the first group in the same experiment ($p < 0.001$, unpaired t-test).

Table 1. Summary of radius and compressibility measurements in this study.

4.3 Measurement of microtubule-disrupted cells

MDA MB231 cells treated with different concentrations of colchicine to disrupt microtubules were tested along with the control group using the compressibility cytometry. All groups were tested under three combinations of input voltage and flow rate, V_I^2/Q = 113.6, 142.5 and 163.6 $V^2(\mu L/min)^{-1}$, which resulted from a constant flow rate Q = 5.5 μL/min and voltages V_I = 25, 28, 30 V.

We observed that the cells also hit the sidewall at certain positions as a result of both acoustics and flow (Fig. 4a). 300~500 cells were tested for each value of V_I^2/Q from each group, and the results were presented as the mean and standard deviation of hitting position for those cells (Fig. 4b). The hitting positions of all groups decreased when the V_I^2/Q increased. At each V_I^2/Q, the mean hitting position of the control group was lower than those of the three colchicine-treated groups, indicating that more control cells hit at earlier positions than the microtubule-disrupted cells.

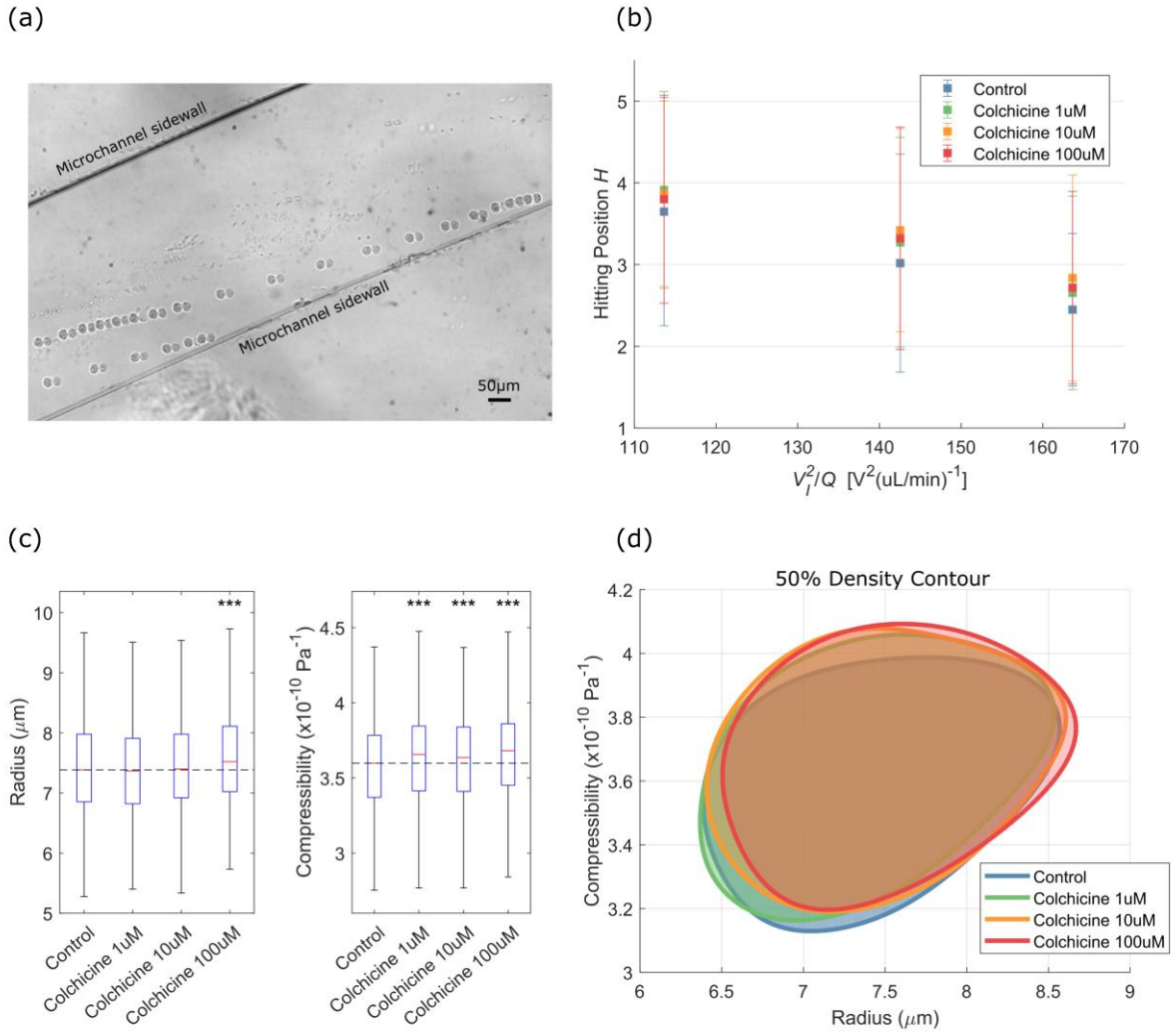

Fig. 4 Measurement of microtubule-disrupted cells. (a) Time-lapse overlaid image of two MDA MB231 cells hitting the sidewall at certain positions as a result of both acoustics and flow. (b) Hitting positions, (c) measured radius and compressibility, and (d) 50% density contour of compressibility *vs* radius for the control (n = 1444), 1 μM colchicine-treated (n = 916), 10 μM colchicine-treated (n = 1013) and 100 μM colchicine-treated (n = 968) cells. *** denotes $p < 0.001$ (unpaired t-test). Data are represented as mean and standard deviation in (b) and a standard box plot in (c). The single cell appeared as double images at every timepoint in (a) due to the uniaxial birefringence of LiNbO3.

The radius and compressibility of control and colchicine-treated cells were measured by the compressibility cytometry (Fig. 4c) and summarised in Table 1. The radius of MDA MB231 cells remained unchanged at 1 μM and 10 μM colchicine treatment and increased at 100 μM colchicine treatment. The compressibility of MDA MB231 cells was increased at all three concentrations, and the cells treated by 100 μM colchicine appeared to be the most

compressible. The 50% density contour of compressibility *vs* radius was plotted for each group (Fig. 4d). From the control to the 100 µM colchicine-treated, the contour of compressibility *vs* radius was gradually shifted upward. It was further shifted to the right at the 100 µM colchicine treatment. The shape of contour did not show a clear difference between groups. The full data of univariate and bivariate distributions of cell compressibility and size can be found in the ESI.

4.4 Measurement of actin-disrupted cells

MDA MB231 cells treated with different concentrations of cytochalasin B to disrupt actin filaments were tested along with the control group using the compressibility cytometry. All groups were tested under three combinations of input voltage and flow rate, V_I^2/Q = 113.6, 142.5 and 163.6 $V^2(\mu L/min)^{-1}$, which resulted from a constant flow rate Q = 5.5 µL/min and voltages V_I = 25, 28, 30 V. The results were presented as the mean and standard deviation of hitting position for those cells (Fig. 5a). The hitting positions of all groups decreased when the V_I^2/Q increased. At each V_I^2/Q, the mean hitting position of the control group was higher than those of the three colchicine-treated groups, showing the opposite trend compared to the colchicine treatment.

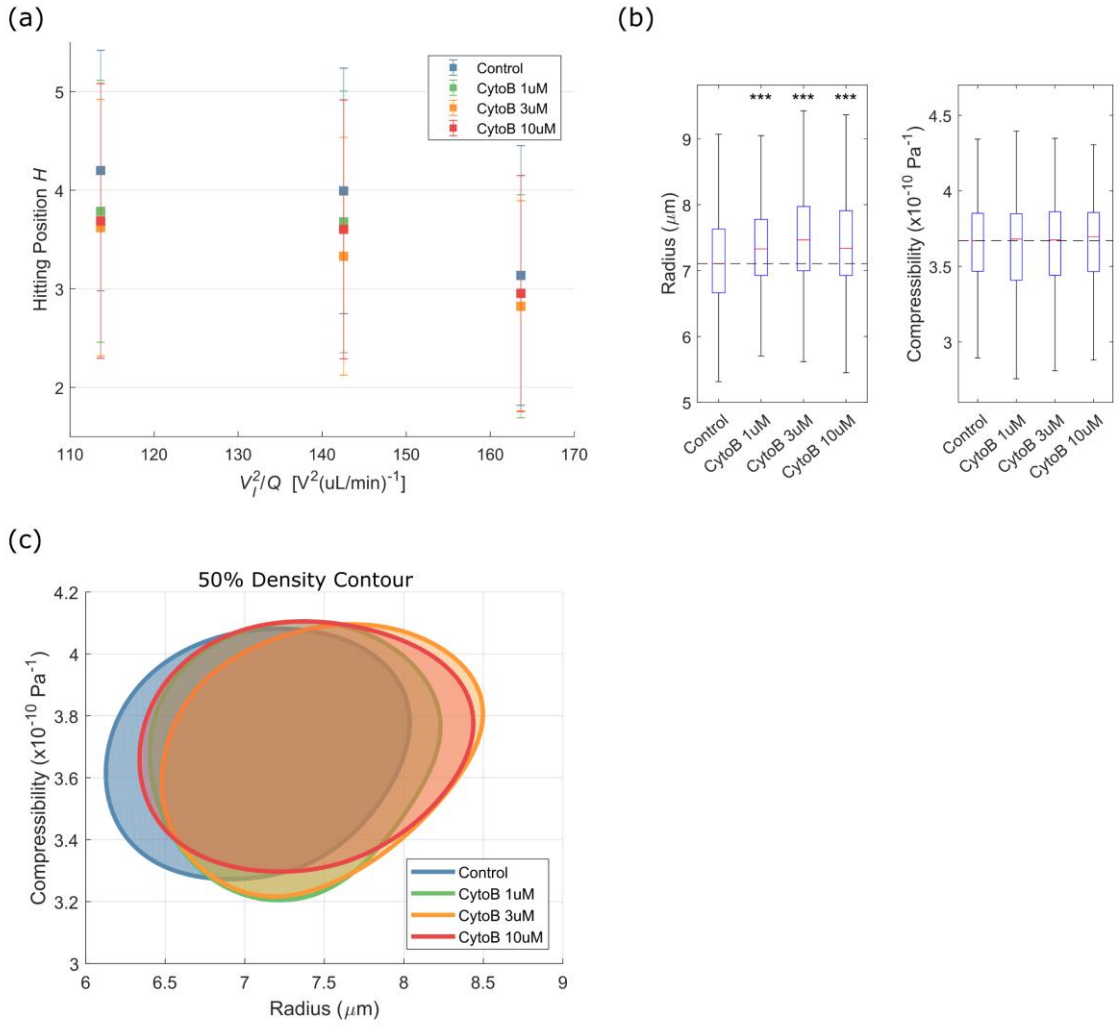

321

Fig. 5 Measurement of actin-disrupted cells. (a) Hitting positions, (b) measured radius and compressibility, and (c) 50% density contour of compressibility *vs* radius for the control (n = 1099), 1 µM cytoB (cytochalasin B) -treated (n = 1016), 3 µM cytoB-treated (n = 989) and 10 µM cytoB-treated (n = 1056) cells. *** denotes $p < 0.001$ (unpaired t-test). Data are represented as mean and standard deviation in (a) and a standard box plot in (b).

322 The radius and compressibility of control and cytochalasin B-treated cells were measured by
323 the compressibility cytometry (Fig. 5b) and summarised in Table 1. The radius of MDA
324 MB231 cells was increased at all three concentrations and the 3 µM treatment had the largest
325 effect on the cell radius. The compressibility of MDA MB231 cells was unchanged at all three
326 concentrations. The 50% density contour of compressibility *vs* radius was plotted for each
327 group (Fig. 5c). The contour of compressibility *vs* radius of all the treatment groups was shifted
328 to the right, as compared to that of the control. The shape of contour at the 1 µM and 3 µM
329 treatments appeared to be wider vertically, indicating a larger variation in compressibility. The

full data of univariate and bivariate distributions of cell compressibility and size can be found in the ESI.

4.5 Measurement of cancer cells with different metastatic potential

MDA MB231 cells and MDA MB231 LNm5 cells which are a highly metastatic variant derived from MDA MB231 cell line were both tested using the compressibility cytometry. The two cell lines were tested under three combinations of input voltage and flow rate, V_I^2/Q = 113.6, 142.5 and 163.6 $V^2(\mu L/min)^{-1}$, which resulted from a constant flow rate Q = 5.5 µL/min and voltages V_I = 25, 28, 30 V.

300~400 cells were tested for each value of V_I^2/Q from each cell line, and the results were presented as the mean and standard deviation of hitting position for those cells (Fig. 6a). The hitting positions of the two cell lines decreased when the V_I^2/Q increased. At each V_I^2/Q, the mean hitting position of MDA MB231 cells was lower than that of MDA MB231 LNm5 cells, indicating that more of the parent cell line hit at earlier position than the highly metastatic daughter line.

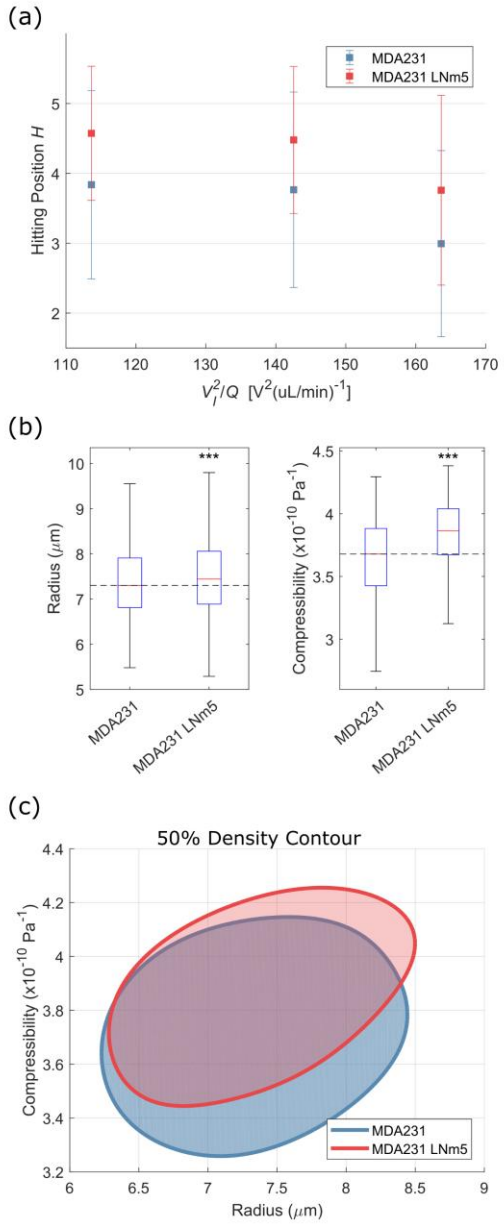

Fig. 6 Measurement of cancer cells with different metastatic potential. (a) Hitting positions, (b) measured radius and compressibility, and (c) 50% density contour of compressibility *vs* radius for MDA MB231 (n = 1197) and MDA MB231 LNm5 (n = 1146) cells. *** denotes $p < 0.001$ (unpaired t-test). Data are represented as mean and standard deviation in (a) and a standard box plot in (b).

The radius and compressibility of MDA MB231 and MDA MB231 LNm5 cells were measured by the compressibility cytometry (Fig. 6b) and summarised in Table 1. The radius and compressibility of the highly metastatic daughter line were both larger than those of the parent cell line. The 50% density contour of compressibility *vs* radius was plotted for each cell line (Fig. 6c). The contour of MDA MB231 LNm5 cells was located higher than that of MDA MB231 cells, suggesting a higher compressibility. In addition, the shape of MDA MB231 LNm5 contour was narrower and the orientation was more towards the top right as compared with MDA MB231 cells, suggesting the different bivariate relationship between compressibility and radius as a characteristic distinguishing the two cancer cell lines that differ

in metastatic potential. The full data of univariate and bivariate distributions of cell compressibility and size can be found in the ESI.

5 Discussion

In this study, we demonstrated a high-throughput compressibility cytometry using multi-tilted-angle SAW, providing thousands of single-cell measurements of compressibility and radius for each cell population. The working principle of compressibility cytometry was studied by mathematical analysis and computational simulation and validated by the experimental results using the microbeads of different materials and sizes. The microbead results also suggest that the compressibility cytometry can detect the difference in material properties such as compressibility between populations. For example, 10-μm PS and 10-μm PMMA microbeads were clearly differentiated in terms of the hitting position in the cytometry and the measured compressibility, while the two populations have no difference in particle size. An error analysis was done to evaluate the compressibility measurement error which was estimated to be 2.5% due to the variations in the calibrated constant C, cell density and radius (see the ESI).

Different cell populations were measured by the compressibility cytometry and the measured compressibility is comparable to the previous acoustofluidic compressibility measurements ranging from 3.28×10^{-10} Pa^{-1} to 4.30×10^{-10} Pa^{-1} for a variety of cell lines.[28,35,36,47] However, the previous studies mostly applied a trajectory-tracking method, which first positioned a target cell away from the pressure node of standing acoustic wave and then exposed the cell to the acoustic wave dragging it to the pressure node. The trajectory of entire time-lapse motion was needed and a slower motion had a better resolution of differentiating small difference.[36] As a consequence, the trajectory-tracking method was implemented under no-flow condition[28,35] or a low flow rate[36] and preferably under low acoustic energy intensity, limiting the throughput and sample size of compressibility measurement. In this study, the compressibility cytometry currently yields a throughput of ~10 cells per second and enables thousands of single-cell compressibility measurements within less than ten minutes for the first time. This is made possible because only the cell count at a hitting position is needed instead of every single-cell trajectory, requiring less instrumental and computational resource and facilitating an easier path towards automation. On the other hand, the large sample size (>1,000 cells) provides more insights on the intrinsic distribution of a cell population and the bivariate correlation between radius and compressibility which significantly differentiated the closely related tumour cell populations used in this study.

The compressibility cytometry also demonstrates a technical improvement from the state-of-the-art SAW-based binary separation. A typical SAW-based binary separation setup is based on a fluidic channel tilted by a constant angle with respect to SAW, similar to the simulation in Fig. 2a. It has demonstrated the effectiveness in the applications such as microbeads of different sizes,[42,43] circulating tumour cell (CTC) separation from blood[42,44,59] and bacteria separation from blood,[60] which benefit from the significant difference in size between target and non-target. However, it was reported that two cell populations may have an overlap in biophysical properties due to the heterogeneity of the population, which would be difficult to address in a binary separation.[37,44,46] In the current study, the compressibility cytometry with multiple tilted angles and therefore multiple "binary separations" can examine the heterogeneous biophysical properties within a cell population, identify the overlapping properties between two populations and detect any populational difference such as shift and skew.

The change in cell compressibility due to the microtubule disruption was effectively captured by the compressibility cytometry, while the actin disruption did not change the compressibility of cells but increased the size. This finding agrees with our previous study investigating the roles of cytoskeletal components on cellular elastic moduli via a combined usage of on-chip SAW and micropipette aspiration devices.[51] In light of the cellular tensegrity model, microtubules are seen as compression-resistant struts contributing to whole-cell compressibility, whereas actin filaments are seen as pre-stressed cables capable of resisting tension and shape distortion.[61,62] As the compressibility cytometry showed better sensitivity in cellular microtubule structure, it could focus on microtubule-related applications using cell compressibility as a biophysical marker for the interior structure, such as diseases associated with the structural alteration of microtubules including cancers[63,64] and neurodevelopmental disorders.[65] For example, microtubule rigidity was reported to influence the formation of microtubule bundles and the efficacy of taxane-based chemotherapeutic drugs treating circulating tumour cells.[64] On the other hand, the compressibility cytometry has also effectively detected the biophysical difference between MDA MB231 cell line and its highly metastatic variant MDA MB231 LNm5 cell line which differ in cellular phenotypes and gene expression.[52,54,66] The results agree with the previous studies that the cancer cell lines with higher invasiveness and metastatic potential have a higher compressibility.[37,67] In addition to the compressibility comparison, the bivariate correlation between radius and compressibility

enabled by the compressibility cytometry could be another indicator for tumour cell characterisation.

The current throughput of ~10 cells per second is much higher than the conventional methods such as atomic force microscopy (~10 – 100 cells per hour)[24] but lower than that reported from another well-known microfluidic method called deformability cytometry (~100 – 1,000 cells per second).[22,68,69] However, as the measured mechanical modulus of cells could vary according to the mechanical force profile,[51,70] we see the compressibility cytometry applying a high-frequency compressional wave onto cells as a complement to the deformability cytometry yielding a shear-induced deformation. On the other hand, the current throughput is mainly limited in data acquisition and has not been maximised yet. In the current setup, the movement of cells from appearing in the field of view (FOV) to hitting the sidewall lasted 0.1 – 0.3 seconds at the flow rate of 5.5 μL/min and was captured as 3 – 10 frames by the camera operating at 30 frames per second. Although the trajectory tracking is not required for data analysis, this number of frames contain the movement information of the cells just before hitting the sidewall and are needed to differentiate multiple cells that concurrently appeared in the FOV. An increase in flow rate in the current setup may lead to fewer frames captured by the camera and therefore indiscernible hitting position of the cells. For future work, a high-speed camera with higher frame rate could alleviate the limitation and allow the usage of higher flow rate. In addition, a change of design with additional outlets that separately collect the cells from each hitting position would eliminate the need of the movement information before hitting the sidewall. It would also open up the possibility of incorporating on-chip cell counter for each outlet which has been reported to have analysed thousands of cells per second[71] or collecting the cells in different groups for following assays. Hence, we anticipate that the future work could improve the throughput by at least 10 folds or more (>100 cells per second) and combine sequential bioassays following the cytometer.

6 Conclusion

In this study, we developed a high-throughput compressibility cytometry using multi-tilted-angle SAW, which was first conceptualised from mathematical and computational simulations and validated by experiments of microbeads of different materials and sizes. The compressibility cytometry enables thousands of single-cell measurements of radius and compressibility within a few minutes. The compressibility cytometry was proven with the capabilities of detecting the structural alteration of cellular microtubules and comparing the

biophysical phenotypes of tumour cell lines with different metastatic potential. In future work, the compressibility cytometry can be exploited in the areas of cell mechanics, microtubule-related diseases, cancer metastasis and cell sorting based on biophysical phenotypes.

Conflicts of Interest

There are no conflicts to declare.

Acknowledgments

We thank Yudi Niu for helping build the simulation model. This work was performed in part at the Melbourne Centre for Nanofabrication (MCN) in the Victorian Node of the Australian National Fabrication Facility (ANFF). We acknowledge financial support from the Australian Research Council (IC17010000016) support of the ARC Centre for Personalised Therapeutics Technologies and the work contained in this study.

References

1 C. R. Ethier and C. A. Simmons, *Introductory Biomechanics From Cells to Organisms*, 2007.
2 K. A. Jansen, D. M. Donato, H. E. Balcioglu, T. Schmidt, E. H. J. Danen and G. H. Koenderink, *Biochimica et Biophysica Acta (BBA) - Molecular Cell Research*, 2015, **1853**, 3043–3052.
3 F. Basoli, S. M. Giannitelli, M. Gori, P. Mozetic, A. Bonfanti, M. Trombetta and A. Rainer, *Front. Physiol.*, 2018, **9**, 1449.
4 S. A. Vanapalli, M. H. G. Duits and F. Mugele, *Biomicrofluidics*, 2009, **3**, 012006.
5 G. Y. H. Lee and C. T. Lim, *Trends in Biotechnology*, 2007, **25**, 111–118.
6 P. Roca-Cusachs, V. Conte and X. Trepat, *Nat Cell Biol*, 2017, **19**, 742–751.
7 M. M. Brandao, A. Fontes, M. L. Barjas-Castro, L. C. Barbosa, F. F. Costa, C. L. Cesar and S. T. O. Saad, *European Journal of Haematology*, 2003, **70**, 207–211.
8 H. W. Hou, A. A. Bhagat, A. G. Chong, P. Mao, K. S. Tan, J. Han and C. T. Lim, *Lab Chip*, 2010, **10**, 2605–2613.
9 C. T. LIM, *Journal of Biomechanical Science and Engineering*, 2006, **1**, 82–92.
10 J. Guck, S. Schinkinger, B. Lincoln, F. Wottawah, S. Ebert, M. Romeyke, D. Lenz, H. M. Erickson, R. Ananthakrishnan, D. Mitchell, J. Kas, S. Ulvick and C. Bilby, *Biophysical Journal*, 2005, **88**, 3689–3698.
11 C. N. Holenstein, A. Horvath, B. Schär, A. D. Schoenenberger, M. Bollhalder, N. Goedecke, G. Bartalena, O. Otto, M. Herbig, J. Guck, D. A. Müller, J. G. Snedeker and U. Silvan, *MBoC*, 2019, **30**, 887–898.
12 R. Krishnan, J. A. Park, C. Y. Seow, P. V. S. Lee and A. G. Stewart, *Trends in Pharmacological Sciences*, 2016, **37**, 87–100.
13 H. T. K. Tse, D. R. Gossett, Y. S. Moon, M. Masaeli, M. Sohsman, Y. Ying, K. Mislick, R. P. Adams, J. Rao and D. Di Carlo, *Science translational medicine*, 2013, **5**, 212ra163.
14 N. O. Petersen, W. B. McConnaughey and E. L. Elson, *Proceedings of the National Academy of Sciences*, 1982, **79**, 5327–5331.
15 E. J. Koay, A. C. Shieh and K. A. Athanasiou, *Journal of Biomechanical Engineering*, 2003, **125**, 334–341.

16 G. Binnig and C. F. Quate, *Physical Review Letters*, 1986, **56**, 930–933.
17 R. M. Hochmuth, *Journal of Biomechanics*, 2000, **33**, 15–22.
18 S. B. Smith, Y. Cui and C. Bustamante, *Methods in Enzymology*, 2003, **361**, 134–162.
19 Q. Xin, P. Li, Y. He, C. Shi, Y. Qiao, X. Bian, J. Su, R. Qiao, X. Zhou and J. Zhong, *Anal. Methods*, 2017, **9**, 5720–5730.
20 M. L. Rodriguez, P. J. McGarry and N. J. Sniadecki, *Applied Mechanics Reviews*, 2013, **65**, 060801.
21 H. W. Hou, W. C. Lee, M. C. Leong, S. Sonam, S. R. K. Vedula and C. T. Lim, *Cel. Mol. Bioeng.*, 2011, **4**, 591–602.
22 O. Otto, P. Rosendahl, A. Mietke, S. Golfier, C. Herold, D. Klaue, S. Girardo, S. Pagliara, A. Ekpenyong, A. Jacobi, M. Wobus, N. Töpfner, U. F. Keyser, J. Mansfeld, E. Fischer-Friedrich and J. Guck, *Nature Methods*, 2015, **12**, 199–202, 4 p following 202.
23 M. Xavier, P. Rosendahl, M. Herbig, M. Kräter, D. Spencer, M. Bornhäuser, R. O. C. Oreffo, H. Morgan, J. Guck and O. Otto, *Integrative biology : quantitative biosciences from nano to macro*, 2016, 10–12.
24 P. Rosendahl, K. Plak, A. Jacobi, M. Kraeter, N. Toepfner, O. Otto, C. Herold, M. Winzi, M. Herbig, Y. Ge, S. Girardo, K. Wagner, B. Baum and J. Guck, *Nat Methods*, 2018, **15**, 355–358.
25 W. G. Lee, H. Bang, H. Yun, J. Lee, J. Park, J. K. Kim, S. Chung, K. Cho, C. Chung, D.-C. Han and J. K. Chang, *Lab on a Chip*, 2007, **7**, 516.
26 J. P. Shelby, J. White, K. Ganesan, P. K. Rathod and D. T. Chiu, *Proceedings of the National Academy of Sciences*, 2003, **100**, 14618–14622.
27 H. W. Hou, Q. S. Li, G. Y. H. Lee, A. P. Kumar, C. N. Ong and C. T. Lim, *Biomedical Microdevices*, 2009, **11**, 557–564.
28 T. Yang, F. Bragheri, G. Nava, I. Chiodi, C. Mondello, R. Osellame, K. Berg-Sørensen, I. Cristiani and P. Minzioni, *Scientific Reports*, 2016, **6**, 23946.
29 H. Kubitschke, J. Schnauss, K. D. Nnetu, E. Warmt, R. Stange and J. Kaes, *New J. Phys.*, 2017, **19**, 093003.
30 G. Destgeer and H. J. Sung, *Lab on a Chip*, 2015, **15**, 2722–38.
31 X. Ding, P. Li, S.-C. S. Lin, Z. S. Stratton, N. Nama, F. Guo, D. Slotcavage, X. Mao, J. Shi, F. Costanzo and T. J. Huang, *Lab on a Chip*, 2013, **13**, 3626.
32 D. J. Collins, B. Morahan, J. Garcia-Bustos, C. Doerig, M. Plebanski and A. Neild, *Nature Communications*, 2015, **6**, 8686.
33 T. D. Nguyen, Y. Q. Fu, V.-T. Tran, A. Gautam, S. Pudasaini and H. Du, *Sensors and Actuators B: Chemical*, 2020, **318**, 128143.
34 H. Bruus, *Lab on a Chip*, 2012, **12**, 1014.
35 D. Hartono, Y. Liu, P. L. Tan, X. Y. S. Then, L.-Y. L. Yung and K.-M. Lim, *Lab on a Chip*, 2011, **11**, 4072.
36 Y. Wu, A. G. Stewart and P. V. S. Lee, *Biomicrofluidics*, 2019, **13**, 024107.
37 H. Wang, Z. Liu, D. M. Shin, Z. G. Chen, Y. Cho, Y.-J. Kim and A. Han, *Lab on a Chip*, 2019, **19**, 387–393.
38 M. Wu, A. Ozcelik, J. Rufo, Z. Wang, R. Fang and T. Jun Huang, *Microsyst Nanoeng*, 2019, **5**, 32.
39 F. Petersson, L. Åberg, A. M. Swärd-Nilsson and T. Laurell, *Analytical Chemistry*, 2007, **79**, 5117–5123.
40 P. Augustsson, C. Magnusson, M. Nordin, H. Lilja and T. Laurell, *Analytical Chemistry*, 2012, **84**, 7954–7962.
41 M. Antfolk, S. H. Kim, S. Koizumi, T. Fujii and T. Laurell, *Sci Rep*, 2017, **7**, 46507.
42 X. Ding, Z. Peng, S.-C. S. Lin, M. Geri, S. Li, P. Li, Y. Chen, M. Dao, S. Suresh and T. J. Huang, *Proceedings of the National Academy of Sciences*, 2014, **111**, 12992–12997.

43 D. J. Collins, T. Alan and A. Neild, *Lab Chip*, 2014, **14**, 1595–1603.
44 P. Li, Z. Mao, Z. Peng, L. Zhou, Y. Chen, P.-H. Huang, C. I. Truica, J. J. Drabick, W. S. El-Deiry, M. Dao, S. Suresh and T. J. Huang, *Proceedings of the National Academy of Sciences of the United States of America*, 2015, **112**, 4970–4975.
45 S. Karthick, P. N. Pradeep, P. Kanchana and A. K. Sen, *Lab Chip*, 2018, **18**, 3802–3813.
46 Y. Xie, Z. Mao, H. Bachman, P. Li, P. Zhang, L. Ren, M. Wu and T. J. Huang, *Journal of Biomechanical Engineering*, 2020, **142**, 031005.
47 A. Riaud, W. Wang, A. L. P. Thai and V. Taly, *Phys. Rev. Applied*, 2020, **13**, 034058.
48 K. Yosioka and Y. Kawasima, *Acta Acustica united with Acustica*, 1955, **5**, 167.
49 E. C. Anderson, D. F. Petersen and R. A. Tobey, *Biophysical Journal*, 1970, **10**, 630–645.
50 A. K. Bryan, V. C. Hecht, W. Shen, K. Payer, W. H. Grover and S. R. Manalis, *Lab on a Chip*, 2014, **14**, 569–576.
51 Y. Wu, T. Cheng, Q. Chen, B. Gao, A. G. Stewart and P. V. S. Lee, *Biomicrofluidics*, 2020, **14**, 014114.
52 E. R. Fietz, C. R. Keenan, G. López-Campos, Y. Tu, C. N. Johnstone, T. Harris and A. G. Stewart, *Sci Rep*, 2017, **7**, 43774.
53 X.-Z. Chang, D.-Q. Li, Y.-F. Hou, J. Wu, J.-S. Lu, G.-H. Di, W. Jin, Z.-L. Ou, Z.-Z. Shen and Z.-M. Shao, *Breast Cancer Res Treat*, 2008, **111**, 65–78.
54 C. N. Johnstone, A. D. Pattison, K. L. Gorringe, P. F. Harrison, D. R. Powell, P. Lock, D. Baloyan, M. Ernst, A. G. Stewart, T. H. Beilharz and R. L. Anderson, *Dis. Model. Mech.*, 2018, **11**, dmm032250.
55 S. MacLean-Fletcher, *Cell*, 1980, **20**, 329–341.
56 S. Hirawa, T. Masudo and T. Okada, *Analytical Chemistry*, 2007, **79**, 3003–3007.
57 K. W. Cushing, F. Garofalo, C. Magnusson, L. Ekblad, H. Bruus and T. Laurell, *Analytical Chemistry*, 2017, **89**, 8917–8923.
58 J. E. Carlson, J. van Deventer, A. Scolan and C. Carlander, *IEEE Symposium on Ultrasonics, 2003.*, 2003, **00**, 885–888.
59 M. Wu, P.-H. Huang, R. Zhang, Z. Mao, C. Chen, G. Kemeny, P. Li, A. V. Lee, R. Gyanchandani, A. J. Armstrong, M. Dao, S. Suresh and T. J. Huang, *Small*, 2018, **14**, 1801131.
60 S. Li, F. Ma, H. Bachman, C. E. Cameron, X. Zeng and T. J. Huang, *J. Micromech. Microeng.*, 2017, **27**, 015031.
61 D. E. Ingber, *Journal of cell science*, 1993, **104**, 613–27.
62 D. E. Ingber, *Journal of Cell Science*, 2003, **116**, 1157–1173.
63 E. Mukhtar, D. Worroll, G. Galletti, S. Schuster, S. A. Piha-Paul and P. Giannakakou, *CDR*, , DOI:10.20517/cdr.2019.116.
64 M. Kim and K. A. Rejniak, *Biophysical Journal*, 2014, **107**, 1236–1246.
65 M. Lasser, J. Tiber and L. A. Lowery, *Front. Cell. Neurosci.*, 2018, **12**, 165.
66 Y. Tu, C. N. Johnstone, J. G. Ryall, G. H. López-Campos, C. R. Keenan and A. G. Stewart, *JCMT*, , DOI:10.20517/2394-4722.2018.67.
67 H. Wang, Z. Liu, D. M. Shin, Z. G. Chen, Y. Cho, Y. J. Kim and A. Han, *Microfluidics and Nanofluidics*, 2018, **22**, 1–7.
68 D. R. Gossett, H. T. K. Tse, S. a. Lee, Y. Ying, a. G. Lindgren, O. O. Yang, J. Rao, a. T. Clark and D. Di Carlo, *Proceedings of the National Academy of Sciences*, 2012, **109**, 7630–7635.
69 K. D. Nyberg, K. H. Hu, S. H. Kleinman, D. B. Khismatullin, M. J. Butte and A. C. Rowat, *Biophysical Journal*, 2017, **113**, 1574–1584.
70 P. H. Wu, D. R. B. Aroush, A. Asnacios, W. C. Chen, M. E. Dokukin, B. L. Doss, P. Durand-Smet, A. Ekpenyong, J. Guck, N. V. Guz, P. A. Janmey, J. S. H. Lee, N. M. Moore, A. Ott,

Y. C. Poh, R. Ros, M. Sander, I. Sokolov, J. R. Staunton, N. Wang, G. Whyte and D. Wirtz, *Nature Methods*, 2018, **15**, 1–8.
71 W. Tang, D. Tang, Z. Ni, N. Xiang and H. Yi, *Anal. Chem.*, 2017, **89**, 3154–3161.

Captions

Fig. 1 (a) Photo of compressibility cytometer, consisting of a pair of interdigital transducers (IDTs) on a LiNbO3 piezoelectric substrate and a PDMS microchannel containing a series of segments tilted by different angles. The grid square in the background is 10 mm × 10 mm. (b) Schematic of compressibility cytometer separating microparticles or cells into different bins by dragging them towards the sidewalls at different segments of the microfluidic channel.

Fig. 2 (a) Simulation of a one-tilted-angle scenario. The lateral displacement was simulated with regard to a range of tilted angle θ and a range of particle compressibility β_P, while the other parameters were fixed. (b) Simulation of multi-tilted-angle compressibility cytometry. The simulated hitting position H is a function of parameter $C\frac{V_I^2}{Q}$ related to a constant C, input voltage V_I and flow rate Q, and particle property ψ related to size, density and compressibility. Results were represented as a hitting position map.

Fig. 3 Measurement of microbeads. (a) Time-lapse overlaid image of two microbeads hitting the sidewall at certain positions as a result of both acoustics and flow. (b) Experimental and predicted hitting positions, (c) measured radius and compressibility, and (d) 50% density contour of compressibility *vs* radius for 10-μm PS (n = 476), 10-μm PMMA (n = 346) and 15-μm PS (n = 314) microbeads. *** denotes $p < 0.001$ (unpaired t-test). Data are represented as mean and standard deviation in (b) and a standard box plot in (c). The single microbead appeared as double images at every timepoint in (a) due to the uniaxial birefringence of LiNbO3.

Fig. 4 Measurement of microtubule-disrupted cells. (a) Time-lapse overlaid image of two MDA MB231 cells hitting the sidewall at certain positions as a result of both acoustics and flow. (b) Hitting positions, (c) measured radius and compressibility, and (d) 50% density contour of compressibility *vs* radius for the control (n = 1444), 1 μM colchicine-treated (n = 916), 10 μM colchicine-treated (n = 1013) and 100 μM colchicine-treated (n = 968) cells. *** denotes $p < 0.001$ (unpaired t-test). Data are represented as mean and standard deviation in (b) and a standard box plot in (c). The single cell appeared as double images at every timepoint in (a) due to the uniaxial birefringence of LiNbO3.

Fig. 5 Measurement of actin-disrupted cells. (a) Hitting positions, (b) measured radius and compressibility, and (c) 50% density contour of compressibility *vs* radius for the control (n = 1099), 1 μM cytoB (cytochalasin B) -treated (n = 1016), 3 μM cytoB-treated (n = 989) and 10

µM cytoB-treated (n = 1056) cells. *** denotes $p < 0.001$ (unpaired t-test). Data are represented as mean and standard deviation in (a) and a standard box plot in (b).

Fig. 6 Measurement of cancer cells with different metastatic potential. (a) Hitting positions, (b) measured radius and compressibility, and (c) 50% density contour of compressibility *vs* radius for MDA MB231 (n = 1197) and MDA MB231 LNm5 (n = 1146) cells. *** denotes $p < 0.001$ (unpaired t-test). Data are represented as mean and standard deviation in (a) and a standard box plot in (b).